Influence of coherent vibrational excitation on the high-order harmonic generation of diatomic molecules

Mohammad Monfared [1,2,*] Elnaz Irani,[1,†] Christoph Lemell [2] and Joachim Burgdörfer[2]
[1]*Department of Physics, Faculty of Basic Sciences, Tarbiat Modares University, P.O. Box 14115-175, Tehran, Iran*
[2]*Institute for Theoretical Physics, Vienna University of Technology, Wiedner Hauptstrasse 8-10, A-1040 Vienna, Austria, EU*

(Received 19 October 2021; revised 19 September 2022; accepted 21 October 2022; published 10 November 2022)

High-order harmonic generation (HHG) in atomic systems by the highly nonlinear response to an intense laser field is a prominent pathway to the synthesis of ever shorter laser pulses at increasingly higher photon energies. Extensions of this process to molecules add to the complexity but also offer novel opportunities as multicenter effects and the coupling to nuclear degrees of freedom can influence HHG. In this paper, we theoretically explore the impact of coherent vibrational excitations of diatomic molecules on the HHG spectrum within the framework of time-dependent density-functional theory. We observe the appearance of interference structures in the HHG spectra controlled by resonances between the driving field and the vibrational wave packet.

DOI: 10.1103/PhysRevA.106.053108

I. INTRODUCTION

High-order harmonic generation (HHG) represents one of the major gateways towards obtaining spatially and temporally coherent extreme ultraviolet radiation light sources with unique properties for a wide range of applications [1–7]. HHG has enabled the study of structural and dynamical information of matter and control of nuclear and electronic dynamics on their natural time scales [8–10]. The nonlinear process of HHG from atoms is well understood in terms of the three-step model [11,12] in which electrons are first released from the ground state of the atom to the continuum by tunneling, are then accelerated by the laser electric field, and finally recombine with the parent ion. Numerical simulations for this process have been performed by a large variety of theoretical methods for solving the time-dependent Schrödinger equation (TDSE) including the single-active electron (SAE) approximation [13,14], the grid-based exact numerical solution of the two-electron TDSE for helium [15–17], time-dependent density-functional theory (TDDFT) [18] applied to multielectron atoms on the mean-field level [19], the multiconfiguration time-dependent Hartree-Fock approach [20] including correlation effects beyond TDDFT, and, more recently, the time-dependent two-particle reduced density matrix method [21] bypassing the need for representing the N-electron wave function.

Extensions to molecular systems pose new challenges as the coupling between electronic and nuclear degrees of freedom and multicenter interference effects have to be included. The extension of the three-step or Lewenstein model [22] to include nuclear degrees of freedom provides a helpful guide and physical insight into the influence of the nuclear motion on the HHG process [23]. Early numerical simulations of HHG in molecular systems have employed the Born-Oppenheimer (BO) approximation, specifically in the fixed-ion approximation with the nuclei placed at the minima of the ground-state BO potential surface. Initially, the effect of nuclear motion on the HHG process was theoretically studied only for small systems employing either the SAE approximation or reduced-dimension models for two-electron molecules (H_2, D_2) [23–29]. These theoretical studies predict that the nuclear motion leads to a reduction of the harmonics yield [23,25]. The signature of nuclear motion has been seen in the time profiles of high-order harmonics from H_2 by Bandrauk *et al.* [26]. For high laser intensities ($I \approx 1$ PW/cm^2) where multielectron processes become important the nuclear motion shortens the part of the attosecond pulse train that originates from ionization of the first electron and facilitates the onset of the contribution from the release of the second electron for longer pulses. For lower laser intensities ($I \approx 0.1$ PW/cm^2), electron excitation due to recollision of the returning electron was observed in the time profile of the attosecond pulse [27,30]. Comparing the experimental HHG signals from H_2 with those from heavier molecules (N_2) as well as the atomic HHG signal from Ar, all three systems of which feature very similar ionization potentials, has demonstrated that, indeed, the nuclear motion between the ionization and recombination steps leads to an effective suppression of the HHG yield and to a broadening of the harmonic signal [31]. Moreover, in addition to the amplitude reduction a frequency modulation, most prominently a redshift of the HHG peaks, has been observed for longer pulses [32,33]. A reduction of the harmonic yield has also been observed in the calculation by Chu and Groenenboom [34] when accounting for the spread of the wave function of the unperturbed vibrational ground state. This approach could reproduce the isotope effect on the HHG spectrum even without explicitly including the motion of nuclei. Moreover, retrieving the nuclear motion of H_2 and D_2 from the harmonic spectra with sub-fs time resolution has been demonstrated theoretically [23] and experimentally [10,35]. Nuclear

*Corresponding author: m.monfared@yahoo.com
†e.irani@modares.ac.ir

motion reconstruction from experimental HHG signals can be achieved by recording either the ratio of harmonic intensities [35] or the observed frequency shift in HHG signals induced by nuclear motion [10]. TDDFT allows the simulation of HHG for large multielectron molecules [36–41]. While most earlier applications used the fixed-ion approximation, more recent implementations have accounted for nuclear motion by solving concurrently the classical equations of motion for the ions within the framework of Ehrenfest dynamics [42–47].

In a pioneering experimental study, Li *et al.* [48] explored in a pump-probe setting the role of molecular motion in HHG in the presence of vibrational excitations rather than in the ground state. Exciting the N–N stretch mode of the N_2O_4 molecule they could identify the dependence of the HHG on the phase of vibration with a peak of HHG emission occurring near the outer turning point of the vibration. Motivated by this advance, we theoretically study in the present paper the effects of the excitation of quasiclassical vibrational wave packets on the HHG spectrum of several diatomic molecules (H_2, N_2, F_2, and HF). We treat the problem in its full dimensionality and include multielectron effects on the level of TDDFT for molecules with up to 14 active electrons. We include the coupling between the electronic and the vibrational degrees of freedom of the nuclei by solving the Kohn-Sham equations of TDDFT in the presence of the classical motion of nuclei determined by the time-dependent mean field. We go beyond this standard Ehrenfest-TDDFT by including quantum effects of the moving and spreading vibrational wave packet on the induced high-order harmonic radiation field. One of our key findings is that resonance structures appear in the HHG spectra of molecules when the frequencies of vibrational motion and of the infrared (IR) laser field driving the electronic dynamics are commensurate to each other.

In Sec. II we review the theoretical background and computational methods employed in our simulations. A comparison between HHG spectra with and without accounting for the nuclear degrees of freedom is given in Sec. III. The case of resonant driving by commensurate frequencies between laser field and coherently excited vibrational wave packets is investigated in Sec. IV. Conclusions drawn from our results are discussed in Sec. V. Atomic units ($e = m_e = \hbar = 1$ a.u.) are used throughout the paper unless stated otherwise.

II. THEORETICAL BACKGROUND AND SIMULATION METHODS

In this section, we briefly review the theoretical background and the implementation of the present simulation of high-order harmonic spectra for multielectron diatomic molecules with the aim to approximately account for the coupling between the electronic and nuclear degrees of freedom. The starting point of the present approach is the well-established Ehrenfest-TDDFT within which the ionic motion follows the classical equations of motion with forces self-consistently determined from the time-dependent electronic density propagated by TDDFT. We go beyond the purely classical description of the ionic motion by accounting for the influence of the motion and shape of the vibrational wave packet on the high-order harmonic generation. We present first applications of this approach to HHG in the presence of the excitation of near-minimum uncertainty Schrödinger (or Glauber) wave packets which closely follow the classical vibrational motion.

A. HHG in diatomic multielectron molecules

We consider diatomic molecules subject to the interaction of strong and short few-cycle laser pulses aligned parallel to the molecular axis ($\hat{z}$) and defined by

$$\vec{E}(t) = E_0\, f_{\rm env}(t)\sin[\omega_L t]\,\hat{e}_z \tag{1}$$

with E_0 the peak electric field, $f_{\rm env}(t)$ the normalized pulse-envelope function, and ω_L the laser frequency. We use pulses with a trapezoidal envelope with one cycle ramp on, 4 to 12 cycles constant amplitude, and one cycle ramp off. We consider in the following moderate laser intensities with peak values $I_0 \leqslant 10^{14}$ W/cm^2 (peak amplitude $E_0 = 0.053$ a.u.) such that the total ionization probability during the interaction with the ultrashort pulses remains small (<0.01%). We vary the infrared wavelength λ_L to probe for resonance effects.

The Hamiltonian of the molecule in the external field is given by

$$H(\underline{\vec{R}}, \underline{\vec{r}}, t) = T_n(\underline{\vec{R}}) + V_{nn}(\underline{\vec{R}}) + H_{\rm el}(\underline{\vec{R}}, \underline{\vec{r}}) + V_{\rm ext}(\underline{\vec{r}}, t) \tag{2}$$

with $\underline{\vec{r}} = (\vec{r}_1, \ldots, \vec{r}_N)$ denoting all electronic coordinates, $\underline{\vec{R}} = (\vec{R}_1, \vec{R}_2)$ the nuclear (or ionic core) coordinates, and

$$V_{\rm ext}(\underline{\vec{r}}, t) = \sum_{i=1}^{N} \vec{r}_i \cdot \vec{E}(t) \tag{3}$$

the interaction with the laser field in dipole approximation and length gauge. $H_{\rm el}(\underline{\vec{R}}, \underline{\vec{r}})$ represents the Hamiltonian of the molecular N-electron system including the electron-nucleus interactions $V_{ne}(\underline{\vec{R}}, \underline{\vec{r}})$, $V_{nn}(\underline{\vec{R}})$ denotes the nucleus-nucleus (or core-core) interactions, and $T_n(\underline{\vec{R}})$ abbreviates the nuclear kinetic energy. In the special case of a diatomic molecule considered in the following, neglecting the rotational degrees of freedom (i.e., for total nuclear angular momentum $\vec{N} = 0$), and focusing on the vibrational degree of freedom, the kinetic energy depends, after separating the center-of-mass motion, only on the relative coordinate $\mathcal{R} = |\vec{R}_1 - \vec{R}_2|$, $T(\mathcal{R})$. The exact solution to the time-dependent Schrödinger equation of the molecule

$$i\frac{\partial}{\partial t}\Psi(\underline{\vec{R}}, \underline{\vec{r}}, t) = H(\underline{\vec{R}}, \underline{\vec{r}}, t)\Psi(\underline{\vec{R}}, \underline{\vec{r}}, t) \tag{4}$$

depends, in general, on all nuclear ($\underline{\vec{R}}$) and electronic ($\underline{\vec{r}}$) coordinates. In the present case, the dependence on coordinates is reduced to $\Psi(\mathcal{R}, \underline{\vec{r}}, t)$.

Using the classical Larmor formula for radiation emitted by accelerated charges well justified for strong-field driven electron dynamics, the high-harmonic spectrum is calculated from the dipole acceleration $a(t) = \ddot{d}(t)$ of the electrons:

$$S(\omega) = \frac{3}{2\pi c^3}|\vec{a}(\omega)|^2. \tag{5}$$

The time-dependent dipole moment (TDDM) $\vec{d}(t)$ is given in terms of the diagonal matrix elements of the electronic dipole

operator by

$$\vec{d}(t) = \langle \Psi(t)| \sum_{i=1}^{N} \vec{r}_i |\Psi(t)\rangle. \tag{6}$$

The frequency dependence of $\vec{d}(t)$ follows from the Fourier transform

$$\vec{d}(\omega) = \frac{1}{T}\int_0^T dt\, e^{-i\omega t}\vec{d}(t) \tag{7}$$

and the acceleration entering Eq. (5) from

$$\vec{a}(\omega) = -\omega^2 \vec{d}(\omega). \tag{8}$$

For later reference, we note that the application of this classical Larmor formula is expected to fail in the perturbative limit and for spontaneous emission accompanied by the radiative decay of excited states [49].

B. Ehrenfest-TDDFT for HHG

The starting point of our approximate treatment of the coupled electronic and nuclear dynamics in the laser-driven diatomic molecule is the *exact* factorization of the time-dependent wave function demonstrated by Gross and coworkers [50,51]:

$$\Psi(\mathcal{R}, \underline{\vec{r}}, t) = \chi(\mathcal{R}, t)\Phi_{\mathcal{R}}(\underline{\vec{r}}, t). \tag{9}$$

Despite the complete factorization at any instance of time reminiscent of the Born-Oppenheimer separation, the time evolution of the nuclear wave function $\chi(\mathcal{R}, t)$ and of the electronic wave function $\Phi_{\mathcal{R}}(\underline{\vec{r}}, t)$ are fully coupled as these wave functions obey a system of coupled effective time-dependent Schrödinger-like equations containing generalized time-dependent potential-energy surfaces and the Berry connection [50,51]. A direct solution of this complicated system of equations has, to our knowledge, not yet been achieved for any realistic multielectron system in three dimensions. The recently introduced time-dependent Born-Oppenheimer (TDBO) approximation [52] also uses a similar factorization [Eq. (9)]. However, while the resulting approximate effective Schrödinger equation for the nuclear wave function $\chi^{\mathrm{TDBO}}(\mathcal{R}, t)$ incorporates information on the motion of the electronic wave packet, the electronic wave function $\Phi^{\mathrm{TDBO}}_{\mathcal{R}}(\underline{\vec{r}}, t)$ is calculated for a given $\mathcal{R}$ treated as a fixed parameter in line with the Born-Oppenheimer assumption that the fast electronic dynamics is approximately decoupled from the much slower nuclear motion. Accordingly, the back coupling of the motion of the nucleus onto the electronic dynamics is neglected.

Using the factorization Eq. (9) the exact TDDM reads

$$\vec{d}(t) = \int d\mathcal{R}\, |\chi(\mathcal{R}, t)|^2 (\Phi_{\mathcal{R}}(\underline{\vec{r}}, t) \left| \sum_{i=1}^{N} \vec{r}_i \right| \Phi_{\mathcal{R}}(\underline{\vec{r}}, t)). \tag{10}$$

Here and in the following, we use rounded brackets to indicate matrix elements in which only the electronic coordinates are integrated over. Note that the exact TDDM [Eq. (10)] can be viewed as the average of the electronic dipole matrix element weighted by the nuclear probability density.

In our simulations we approximate the electronic wave packet in terms of a TDDFT solution, i.e., $\Phi_{\mathcal{R}}(\underline{\vec{r}}, t) \simeq \Phi^{\mathrm{TDDFT}}_{\mathcal{R}}(\underline{\vec{r}}, t)$. Accordingly, the electronic wave function is represented by a Slater determinant of time-dependent single-particle Kohn-Sham (TDKS) orbitals $\phi_i(\vec{r}, t)$. The latter are the solutions of the single-particle TDKS equations

$$i\frac{\partial}{\partial t}\phi_i(\vec{r}, t) = \left[-\tfrac{1}{2}\nabla^2 + V_{\mathrm{H}}(\vec{r}, t) + V_{\mathrm{xc}}(\vec{r}, t) + V_{ne}(\vec{r}, \vec{R}_1, \vec{R}_2, t) + V_{\mathrm{ext}}(\vec{r}, t)\right]\phi_i(\vec{r}, t). \tag{11}$$

In Eqs. (11), $V_{\mathrm{H}}(\vec{r}, t)$ and $V_{\mathrm{xc}}(\vec{r}, t)$ are the Hartree and exchange-correlation potentials, respectively, self-consistently determined by the time-dependent electronic density $n(\vec{r}, t)$ which for a system containing N electrons is given by

$$n(\vec{r}, t) = \sum_{i=1}^{N} |\phi_i(\vec{r}, t)|^2. \tag{12}$$

For V_{ne} we use the Hartwigsen-Goedecker-Hutter pseudopotentials in local-density approximation (LDA) for H_2, N_2, and HF [53] and for F_2 an optimized norm-conserving Vanderbilt pseudopotential in the Perdew-Burke-Ernzerhof generalized gradient approximation (GGA) [54,55]. As described in more detail below, self-interaction corrections (SICs) are included in most of the cases considered. The interaction of the electron with the external field $V_{\mathrm{ext}}(\vec{r}, t)$ is given by Eq. (3). The present TDDFT implementation employs the software package OCTOPUS [56,57]. In order to prevent unphysical reflections of the liberated electron from the boundary of the computing box, the Kohn-Sham orbitals $\phi_i(\vec{r}, t)$ are multiplied with a masking function which is unity in the inner simulation region and is gradually switched off approaching zero at the borders. The width of the masking function is set to 40 a.u. in the direction of the laser polarization and 10 a.u. for the perpendicular directions; the total box size is 300 a.u. along and 80 a.u. perpendicular to the molecular axis. Convergence of the calculations with respect to grid parameters, range of the masking function, and time step has been thoroughly tested and verified.

Approximating the vibrational wave packet $\chi(\mathcal{R}, t)$ by the stationary vibrational ground state $\chi_0(\mathcal{R})$ of the molecule reduces Eq. (10) to

$$\vec{d}(t) = \int d\mathcal{R}\, |\chi_0(\mathcal{R})|^2 \sum_{i=1}^{N} \left(\phi^{\mathrm{TDDFT}}_{i,\mathcal{R}}(\vec{r}, t)|\vec{r}|\phi^{\mathrm{TDDFT}}_{i,\mathcal{R}}(\vec{r}, t)\right) \tag{13}$$

where i labels the TDKS orbital and $\mathcal{R}$ indicates the dependence on the nuclear coordinate. This expression agrees with the result given by Chu and Groenenboom [34]. It accounts for the spread in $\mathcal{R}$ of the vibrational wave function while it neglects the influence of the motion of the nuclear wave packet on the electronic dynamics. One salient feature of Eq. (13) is that the amplitude of the resulting harmonic radiation field is constructed by a coherent superposition of the electronic dipole response evaluated for different $\mathcal{R}$ representing the vibrational quantum state. Therefore, the effect of position and shape of the vibrational wave function on the HHG is approximately accounted for, as evidenced by the ability to reproduce the isotope effect on HHG [34]. As pointed out there, this approach can be viewed as the description of HHG

in terms of independent quantum dynamics of electronic and nuclear degrees of freedom applicable in the regime of weak coupling between the two.

Inclusion of the coupling between nuclear and electronic degrees of freedom on a classical level can be accounted for by Ehrenfest-TDDFT. This approximation to the TDDM follows from Eq. (10) by the substitution

$$|\chi(\mathcal{R},t)|^2 \simeq \delta[\mathcal{R}-\mathcal{R}_c(t)], \tag{14}$$

i.e., by approximating the nuclear wave packet by a δ-peaked distribution centered at the classical trajectory $\mathcal{R}_c(t)$. The resulting TDDM now reads

$$\vec{d}(t) = \sum_{i=1}^{N} \left(\phi^{\mathrm{TDDFT}}_{i,\mathcal{R}_c(t)}(\vec{r},t)|\vec{r}|\phi^{\mathrm{TDDFT}}_{i,\mathcal{R}_c(t)}(\vec{r},t)\right). \tag{15}$$

The classical vibrational motion $\mathcal{R}_c(t) = |\vec{R}_1(t) - \vec{R}_2(t)|$ is determined by solving Newton's equation of motion for the nuclei

$$M_\beta \ddot{\vec{R}}_\beta = -\int n(\vec{r},t)\frac{\partial V_{ne}(\vec{r},\vec{R}_1,\vec{R}_2,t)}{\partial R_\beta}\,d\vec{r} - \frac{\partial V_{nn}(\vec{R}_1,\vec{R}_2)}{\partial R_\beta} + Q_\beta \vec{E}(t) \tag{16}$$

in the presence of the ion-electron potential V_{ne}, the shielded internuclear Coulomb repulsion V_{nn}, and the interaction of the nuclei with the external field. The coupled system of equations of motions for the electronic [Eq. (11)] and the nuclear degrees of freedom [Eq. (16)] is solved concurrently and self-consistently. We employ nuclear pseudopotentials [53,55] to calculate V_{nn}. In Eq. (16), $\vec{R}_\beta$, M_β, and Q_β are the positions, masses, and effective core charges of the nuclei ($\beta = 1, 2$), respectively. The time dependence of the TDDM [Eq. (15)] incorporates, on a classical level, the influence of the nuclear motion on the electronic dynamics and, thus, non–Born-Oppenheimer effects but neglects the spread of the nuclear wave packet. Conversely, back action of the driven electronic dynamics on the ionic motion is taken into account on the mean-field level [$\sim n(\vec{r},t)\frac{\partial}{\partial \mathcal{R}}V_{ne}$] but not on the level of state-specific potential surfaces. The latter appears to be well justified for the present scenario as the overall depopulation of the electronic ground state by the short pulse remains small. Moreover, the excursion of the small fraction of electrons that are tunnel ionized, subsequently accelerated by the laser field, and finally recombine to the electronic ground state proceeds on an ultrashort time scale $\approx 0.7\,T_0$ (T_0: period of the optical field) as estimated for the so-called short trajectories by the semiclassical three-step model [11,12,22]. This time scale corresponds to only a small fraction of a typical ground-state vibrational period T_Ω with Ω the vibrational frequency. During this short time window, ionic cores travel only distances small compared to the spatial spread of the vibrational wave function (see below). Consequently, uncertainty in the potential curves the ions move on has little impact on the nuclear motion on such short time scales, with the possible exception of the lightest molecule H_2 where the deviation between the motion of the protons on the H_2 and H_2^+ potential curves can be larger.

C. HHG in the presence of coherent vibrational excitations

In the following, we extend the description of HHG by Ehrenfest-TDDFT to the case of a molecule prepared in a coherently excited state. We focus in particular on a class of nondispersive (near) minimum-uncertainty wave packets first proposed by Schrödinger for the harmonic oscillator [58] and subsequently extensively employed in the field of quantum optics [59]:

$$\chi_{\alpha(t)}(\mathcal{R}) = e^{-i\Omega t/2}e^{-|\alpha|^2/2}\sum_{\nu=0}^{\infty}\frac{\alpha(t)^\nu}{\sqrt{\nu!}}\chi_\nu(\mathcal{R}) \tag{17}$$

with Ω the vibrational frequency, $\alpha(t) = |\alpha|e^{-i(\Omega t+\phi)}$, $|\alpha| = |\delta\mathcal{R}(t)|_{\max}/\sigma$ the amplitude of excitation in units of the width σ of the wave packet, $|\delta\mathcal{R}(t)|_{\max}$ the maximum of $|\mathcal{R}_c(t) - \mathcal{R}_{eq}|$, and χ_ν the stationary excited vibrational state ν. The amplitude $|\alpha|$ fulfills the inequality $|\alpha| = \sqrt{\langle E\rangle/\Omega} \geqslant \frac{1}{\sqrt{2}}$. The states Eq. (17) are often referred to as Glauber states or coherent states. It should be noted that coherence in the vibrational degree of freedom encoded in Eq. (17) is *a priori* unrelated to the coherence of the superposition of dipole accelerations forming the HHG spectrum. The expression Eq. (17), applicable close to the bottom of the potential-energy curve, can be generalized to anharmonic Morse potentials approximating the BO potential surface for higher excitations [60–63] with increasing $|\alpha|$ probing effects of the anharmonicity of the potential. The motivation for investigating this particular class of wave packets is twofold: On the methodological level, Glauber states represent quantum wave packets bearing the closest resemblance to classical vibrations. Since Ehrenfest-TDDFT [Eq. (16)] accounts only for classical vibrational motion, Glauber states are best suited to preserve classical-quantum correspondence for the interplay between electronic and nuclear motion in these simulations. Moreover, Glauber states are expected to provide a reasonable approximation to impulsively excited vibrational wave packets generated by ultrashort collisional or laser excitation. Vibrational wave packets have been excited by an ultrashort femtosecond pump pulse [64], by $\mathcal{R}$-dependent depletion [65], bond softening [66,67], or stimulated Raman scattering [48]. In such scenarios, the initial (near) Gaussian vibrational ground state is impulsively mapped onto a coherent superposition of a broad distribution of vibrational states on (mostly) excited electronic potential surfaces. In such a (near) vertical sudden Franck-Condon transition the shape of the initial vibrational wave function is approximately conserved. The resulting vibrational wave packet can thus mimic quasiclassical vibrations and, thus, Glauber states as first demonstrated in a pioneering experiment by Dantus *et al.* [64]. Quantitative deviations from the detailed form of Glauber states are, of course, present but are of minor importance on the ultrafast time scale ($\lesssim T_0$) relevant for HHG. The first experimental investigation of HHG in the presence of a quasiclassical vibrational wave packet generated in a pump-probe setting recently presented by Li *et al.* [48] stimulated in part the present investigation.

An example of such a (near) minimum uncertainty vibrational wave packet as employed in our calculations is shown in Fig. 1. To first order, anharmonic corrections can be accounted for by a time-dependent width $\sigma(t) =$

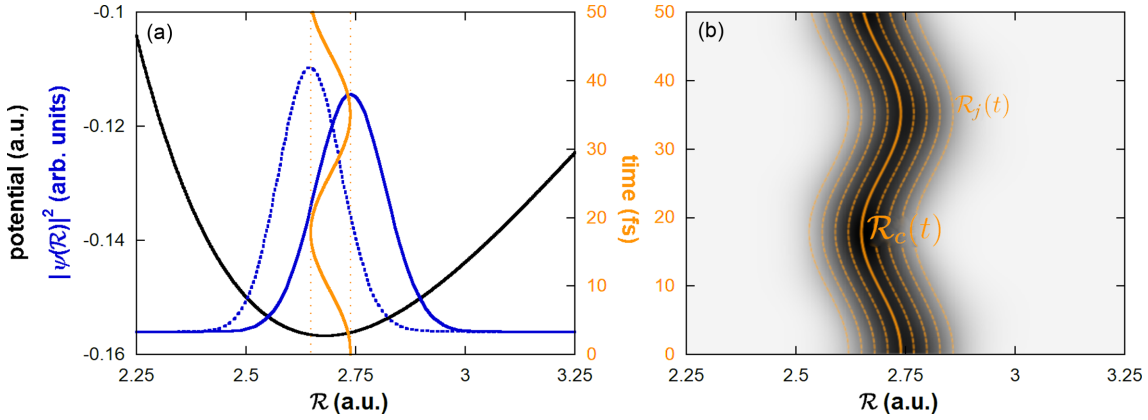

FIG. 1. (a) Morse-type molecular potential curve for F_2 (thick black line) and coherent vibrational wave packet at turning points (dotted and solid blue/dark gray lines). Temporal evolution of expectation value $\langle\mathcal{R}(t)\rangle$ [or Ehrenfest trajectory $\mathcal{R}_c(t)$, orange/light gray solid line; time in fs on right axis]. (b) Trajectories $\mathcal{R}_j(t)$ (thin dashed orange lines) close to the Ehrenfest trajectory $\mathcal{R}_c(t)$ (thick solid orange/light gray line) sampling the wave function of the vibrational wave packet, schematically.

$\sigma[1 + c\,\sin(\Omega t + \phi)]$ of the quantum wave packet. The change of $\sigma(t)$ is obviously synchronized with the vibration. We have performed wave-packet-propagation simulations in the internuclear potential to extract the values for $\sigma(t)$, c, and ϕ for the molecules studied here.

The influence of the coherently excited nuclear wave packet on the HHG can now be accounted for by inserting Eq. (17) into Eq. (10):

$$\vec{d}(t) = \int d\mathcal{R}\,|\chi_{\mathcal{R}_c(t)}(\mathcal{R},t)|^2 \sum_{i=1}^{N} \times \left(\phi_{i,\mathcal{R}}^{\mathrm{TDDFT}}(\vec{r},t)|\vec{r}|\phi_{i,\mathcal{R}}^{\mathrm{TDDFT}}(\vec{r},t)\right) \tag{18}$$

with $\alpha(t) \propto \mathcal{R}_c(t) = \langle\mathcal{R}(t)\rangle$ the expectation value of the wave packet. The time dependence of the nuclear probability density $|\chi_{\mathcal{R}_c(t)}(\mathcal{R},t)|^2$ incorporates both the motion of the center of mass, $\mathcal{R}_c(t)$, of these Glauber states closely following the quasiclassical oscillations of the vibrational degree of freedom as well as their varying width $\sigma(t)$ (Fig. 1). Equation (18) can be viewed as an extension of Ehrenfest-TDDFT that includes now quantum properties of the nuclear wave packet. While the center of the wave packet $\mathcal{R}_c(t)$ follows the concurrently determined classical trajectory in the field of the moving electronic charge cloud, the time-varying distribution of the nuclear probability density is now included, similar to the stationary case [Eq. (13)]. We emphasize that the present extension of Ehrenfest-TDDFT to vibrational wave packets [Eq. (18)] is not limited to Glauber states.

In the numerical implementation of Eq. (18) we sample the time-dependent probability distribution contributing to the dipole moment by a discrete set of $M = 2k + 1$ trajectories $\mathcal{R}_j(t)$ [Fig. 1(b)]:

$$\vec{d}(t) = \sum_j \Delta\mathcal{R}(t)\,|\chi_{\mathcal{R}_c(t)}(\mathcal{R}_j(t),t)|^2 \sum_i^N \times \left(\phi_{i,\mathcal{R}_j(t)}^{\mathrm{TDDFT}}(\vec{r},t)|\vec{r}|\phi_{i,\mathcal{R}_j(t)}^{\mathrm{TDDFT}}(\vec{r},t)\right) \tag{19}$$

with

$$\mathcal{R}_j(t) = \mathcal{R}_c(t) + \Delta\mathcal{R}_j(t), \quad j = -k,\ldots,k \tag{20}$$

the displacement relative to the center (or classical) coordinate $\mathcal{R}_c(t)$ of the wave packet,

$$\Delta\mathcal{R}_j(t) = \Delta\mathcal{R}(t)j. \tag{21}$$

In our calculations the vibrational wave function was scanned in steps of $\Delta\mathcal{R}(t) = \sigma(t)/2$ or (for small $k \leqslant 3$) $\sigma(t)$. For each trajectory $\mathcal{R}_j(t)$ we determine the electronic response in terms of $n[\vec{r},t]$ by solving the TDKS equations [Eq. (11)] and calculate the TDDM from which the frequency-dependent dipole acceleration $a(\omega)$ can be extracted via Eqs. (7) and (8). The dependence of the resulting harmonic radiation [Eq. (5)] on the number of $M = 2k + 1$ sampled trajectories will be investigated below.

For gaining more detailed insights into the timing of the spectral response and the influence of electronic and vibrational dynamics on it, we also perform a time-frequency analysis computing the Gabor transform (windowed Fourier transform) of the dipole acceleration [68,69],

$$\vec{A}(t,\omega) = \int_{-\infty}^{\infty} \ddot{\vec{d}}(t')\exp(-i\omega t')\exp\left[\frac{(t'-t)^2}{2\sigma_\tau^2}\right]dt', \tag{22}$$

with the temporal width σ_τ of the window function (full width at half maximum duration $2\sigma_\tau\sqrt{2\ln 2} \approx 2.35\,\sigma_\tau$).

III. COMPARISON BETWEEN FIXED AND MOVING NUCLEI

In this section we present the results of our simulations performed for the homonuclear molecules H_2, N_2, and F_2 and the heteronuclear molecule HF. We start with examining the self-consistently determined ground-state parameters and discuss the generation of high-order harmonics in molecules with fixed and moving nuclei. While TDDFT is appropriate for multielectron molecules, its applications to H_2 primarily serve as a test case for the interplay between the electronic and ionic dynamics in the presence of fast and large-amplitude

TABLE I. Comparison between calculated and measured values for equilibrium distances, vibrational frequencies, and binding energies of the highest occupied molecular orbitals (HOMO) for the diatomic molecules used in this paper.

	R_{eq} (a.u.)	Ω (a.u.)	HOMO (a.u.)	HOMO-1 (a.u.)	HOMO-2 (a.u.)
			H_2		
Expt.	1.400	2.01×10^{-2}	0.5669		
SIC-LDA	1.311	2.26×10^{-2}	0.6834		
			N_2		
Expt.	2.075	1.06×10^{-2}	0.5726	0.6233	0.6883
SIC-LDA	1.948	1.33×10^{-2}	0.6058	0.6918	0.6992
			F_2		
Expt.	2.668	4.18×10^{-3}	0.5832	0.6910	0.7750
SIC-LDA	2.152	7.2×10^{-3}	0.5428	0.8275	0.9682
GGA	2.68	4.38×10^{-3}	0.3471	0.4697	0.5696
GGA/SIC-GGA			0.5681	0.7034	0.8139
			HF		
Expt.	1.732	1.88×10^{-2}	0.5898	0.7284	1.4545
SIC-LDA	1.667	1.99×10^{-2}	0.6212	0.7613	1.3665

vibrations with, compared to the other molecules, higher frequency and larger amplitude.

A. Equilibrium conditions

We have first tested the accuracy of the stationary DFT predictions for ground-state properties of the investigated molecules before using the same functionals in the subsequent TDDFT simulations. A geometry-optimization calculation was performed to obtain the relaxed coordinates or, equivalently, the equilibrium internuclear distance $\mathcal{R}_{eq}$ for the cores which are then used to determine the electronic ground state as well as the effective internuclear Morse-like potential. As can be seen from Table I experimental binding energies, equilibrium distances, and vibrational frequencies are in most cases reasonably well reproduced using the SIC-LDA exchange-correlation potential. Calculated equilibrium distances $\mathcal{R}_{eq}$ are found to be slightly smaller and, correspondingly, vibrational frequencies Ω slightly larger than measured in experiment in agreement with previous calculations [46]. However, significant deviations are found for the F_2 molecule when using SIC-LDA. Moreover, we did not succeed in finding a single V_{xc} which simultaneously and satisfactorily reproduces electronic and vibrational properties of this molecule. Good agreement between experimental and simulated vibrational properties was found for a GGA potential, while electronic properties were well reproduced using a GGA when including the self-interaction corrections. We therefore dropped the requirement of self-consistency between electronic and ionic potentials built into Ehrenfest-TDDFT for the F_2 molecule. Instead, we first perform a GGA calculation to obtain $\mathcal{R}_{eq}$ and Ω (Table I). Next, we determine $\mathcal{R}_c(t)$ by solving Eq. (16) using the time-dependent potentials generated by a TDDFT calculation employing the GGA functional. Finally, the TDKS equations [Eq. (11)] are solved using the GGA-SIC potential and V_{ne} derived from $\mathcal{R}_c(t)$ recorded in the previous step. This drop of the self-consistency condition on the potentials involved appears to be well justified for the calculation of the HHG for heavier molecules since, on the one hand, the influence of the error in the time-dependent electronic density on the ionic motion via Eq. (16) on such short time scales is small while, on the other hand, the time-dependent change of the ionization potential due to changes of $\mathcal{R}(t)$ has a large influence on the ionization probability and, thus, on the intensity of HHG. It is therefore advantageous to represent $\mathcal{R}(t)$ as accurately as possible. This iteration termed in the following GGA/SIC-GGA resulted in an accuracy of better than 5% for all nuclear and electronic observables (Table I).

The predictions for the internuclear distance $\mathcal{R}(t)$ for H_2 as a function of time with and without including the driving laser field are shown in Fig. 2. For this light molecule, the vibrational oscillation amplitude and the influence of the laser field are the largest. For the heavier molecules investigated in this paper, these effects are considerably smaller. The results of Figs. 2(a) and 2(b) are calculated by Ehrenfest TDDFT, i.e., by self-consistently solving the TDKS equations [Eq. (11)] for the electronic degrees of freedom and Newton's equations of motion [Eq. (16)] for the nuclear degree of freedom. The interaction with the laser field only slightly increases the vibrational amplitude and, correspondingly, decreases the oscillation frequency [Fig. 2(a)]. The latter is an immediate consequence of the anharmonicity explored for increased initial excitation amplitudes $\mathcal{R}(t=0) - \mathcal{R}_{eq} = |\alpha|\sigma$. The increasing anharmonicity is accompanied by an increase of the mean $\langle\mathcal{R}\rangle$, the temporal average over $\mathcal{R}(t)$ over one oscillation period.

In order to estimate possible uncertainties introduced by the mean-field potential of Ehrenfest-TDDFT on the simulation of HHG, we have performed a classical simulation of the nuclear trajectory which follows state-specific potential curves. Implementing the scenario of the three-step model for HHG [11,12], the trajectory initially follows the mean-field force [Eq. (16)] until ionization near the field maximum occurs. At this instant, the trajectory switches to the force field of F_2^+ (mimicking Tully hopping [70]) for about 3/4 of an optical cycle [shaded area in Fig. 2(c)] after which recombination and return to the F_2 potential surface occur. Ionization does, indeed, modify the trajectory, however the displacement in $\mathcal{R}(t)$ relative to the mean-field trajectory by

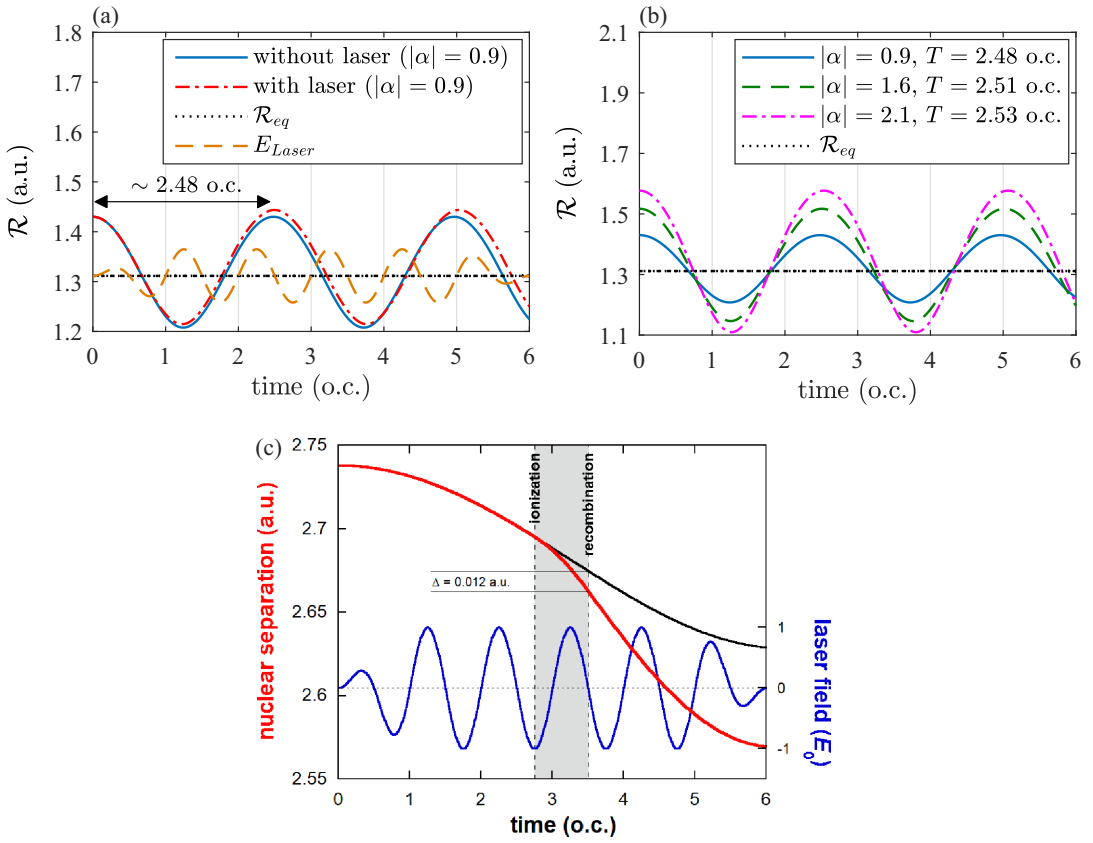

FIG. 2. (a) Comparison between the time-dependent internuclear distance $\mathcal{R}(t)$ of H_2 in the presence (red dash-dotted line) and absence (blue solid line) of the IR laser field ($\lambda_L = 800$ nm, $I_0 = 10^{14}$ W/cm^2) as a function of time in units of optical cycles (o.c.). For illustrative purposes, the amplitude of the laser field is also displayed (in arbitrary units, orange dashed line). For later reference, we note that the frequencies are approximately commensurate, $\omega_L/\Omega \approx 5/2$. The equilibrium distance $\mathcal{R}_{eq} = 1.31$ a.u. predicted by SIC-LDA is also shown for reference. (b) Time-dependent $\mathcal{R}(t)$ for field-free evolution predicted by Ehrenfest-TDDFT for varying initial excitation amplitude $\mathcal{R}(0) - \mathcal{R}_{eq} = |\alpha|\sigma$ to probe for effects of anharmonicity. The legend in the inset denotes the changes of the vibration period. (c) Example of a trajectory $\mathcal{R}_c(t)$ for F_2 in the laser field when $\mathcal{R}_c(t)$ initially follows the mean field but intermittently propagates on the F_2^+ potential curve (Tully hopping [70]) during the excursion of the electron following tunnel ionization at $t = 2.75$ optical cycles, acceleration, and recombination at $t = 3.5$ optical cycles (in red/dark gray). The black line indicates the Ehrenfest trajectory for molecular vibration on the F_2 potential-energy surface without Tully hopping.

the time of recombination is negligibly small compared to the width of the nuclear wave packet [for the example in Fig. 2(c) the displacement is about 1/100 a.u.; cf. Fig. 1]. Later parts of the nuclear trajectory where the displacement gets larger do not affect the HHG spectrum as the probability for multiple ionization within one laser pulse is very small ($\approx 10^{-5}$).

B. Convergence of wave-packet sampling

The spectral amplitude of high-order harmonic radiation $S(\omega)$ [Eq. (5)] is governed by a coherent superposition of dipole accelerations for different trajectories $\mathcal{R}_j(t)$ sampling the vibrational wave packet [Eq. (19)]. Since for computational reasons only a limited number of trajectories can be sampled in the simulation we have tested for the convergence of the final HHG spectrum as a function of the number of sampled trajectories representing the vibrational wave function. We focus in this test on results for the lightest molecule H_2 with the largest vibration frequency for which the HHG spectrum is expected to be most sensitive to the sampling error. For the heavier molecules faster convergence is realized.

Figure 3 displays the harmonic spectra for H_2 as a function of the number $M = 2k + 1$ of coordinates and trajectories sampled both for the vibrational ground state (left) and for a quasiclassical vibration (right), respectively. As reference we show spectra for $\mathcal{R}_{eq}$ (left) and $\mathcal{R}_c(t)$ (right) each without sampling the vibrational wave function [corresponding to $M = 1$ ($k = 0$)]. With increasing M (up to $M = 13$) we observe a clear reduction of the harmonic intensity with increasing number of sampling points. This is related to the rapidly varying phase of a given single harmonic as a function of the internuclear distance shown in Fig. 4 for the case of fixed nuclei. The phase variations strongly increase with harmonic order covering almost the full interval $[0, 2\pi]$ for harmonic 13 when $\mathcal{R}$ is varied over one σ of the width of the ground state. The convergence for the yield of different harmonic orders is presented in Fig. 5 for both fixed (left) and moving nuclei (right). Typically, for $M \gtrsim 5$ a reasonable level of convergence is reached. Convergence is faster for moving nuclei (right) than for fixed nuclei (left) since the time variation $\mathcal{R}(t)$ of individual trajectories effectively aids in the sampling of the $\mathcal{R}$ distribution [Fig. 1(b)]. As the main

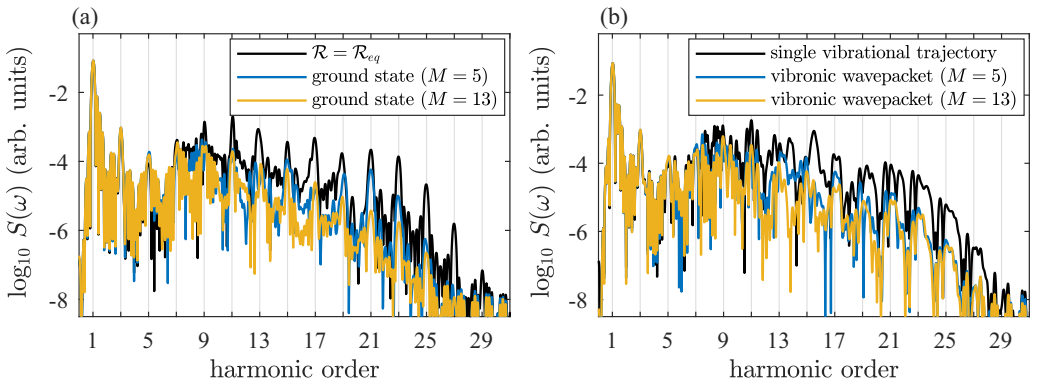

FIG. 3. Harmonic spectra of H_2 driven by a six-cycle laser pulse ($\lambda_L = 742$ nm, $I_0 = 10^{14}$ W/cm^2). (a) Comparison between spectra for fixed nuclei at $\mathcal{R} = \mathcal{R}_{\rm eq}$ and for sampling of the vibrational ground-state wave function with 5 (blue/dark gray) and 13 (orange/light gray) sampling points $\mathcal{R}_i$. (b) Comparison between single Ehrenfest trajectory $\mathcal{R}_c(t)$ starting at the outer turning point $\mathcal{R}_c(t=0) = \mathcal{R}_{\rm eq} + |\alpha|\sigma$ with $|\alpha| = 0.9$ and sampling over a Schrödinger minimum uncertainty wave packet with 5 (blue) and 13 (orange) sampling trajectories $\mathcal{R}_j(t)$.

results of the present paper are not sensitively dependent on the precise value of the harmonic yield, the spectra presented below are mostly calculated for $M = 5$ ($k = 2$).

C. High-order harmonic spectra

Changes in the high-order harmonic spectra of F_2 when the nuclear degrees of freedom are taken into account at various levels of approximation are illustrated in Fig. 6. Remarkably, for this somewhat heavier molecule the HHG spectra resulting from three different approximations closely agree with each other, indicating that, overall, the modulus and phase of the dipole acceleration amplitude $a(\omega)$ [Eq. (8)] vary relatively little with $\mathcal{R}$ over the extent of the vibrational ground-state wave function or, alternatively, over the range of $\mathcal{R}$ covered by the classical vibration. We note that the peak near $8\omega_L$ is not directly associated with the strong-field driven HHG process, the focus of the present paper. Instead, this spectral feature is associated with the energy spacing of the HOMO to an unoccupied molecular DFT orbital in F_2 with a nonvanishing transition dipole moment. Because of the Fourier broadening of the neighboring harmonic peaks by the ultrashort pulse this spectral region becomes accessible. The distinction to the standard HHG spectrum becomes directly visible in the time-frequency spectrum (Gabor transform). The HHG peaks can be identified by their characteristic ω-τ relation (dashed white lines for "short" trajectories). The latter is a hallmark of electron emission, acceleration, and recombination every $\approx 3/4$ of an optical cycle after a field maximum as incorporated in the semiclassical three-step model for HHG [11,12,22]. By contrast, the peak at $8\omega_L$ features no pronounced sub-(optical) cycle structure [Figs. 6(c) and 6(d)] but extends more or less uniformly over the entire pulse duration. As mentioned above, the classical Larmor expression [Eq. (5)] employed in the present HHG simulation is not well suited to accurately describe spontaneous or stimulated bound-bound transitions. Therefore, the quantitative significance of the observed peak near $8\omega_L$ is limited.

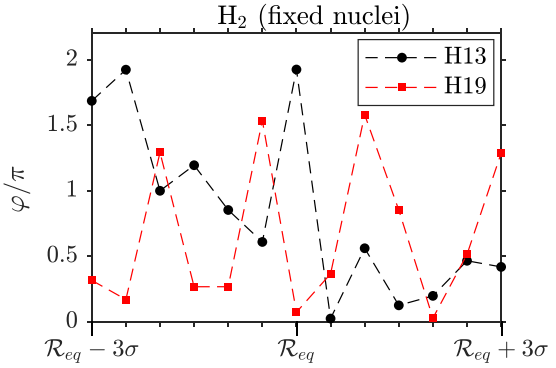

FIG. 4. Variation of the phase $\varphi = \arg[a_{\mathcal{R}}(\omega)]$ of harmonics H13 and H19 as a function of the fixed internuclear distance $\mathcal{R}$ over a large range of $\mathcal{R}$ values covering $\pm 3\sigma$ of the width of the wave packet.

For the lightest molecule, H_2, the influence of the nuclear motion on the electronic dynamics is expected to be most pronounced. Indeed, sampling the stationary vibrational ground-state wave function [Eq. (13)] reduces the harmonic spectrum considerably compared to the fixed-ion result with $\mathcal{R} = \mathcal{R}_{\rm eq}$ [Fig. 3(a)]. This reduction becomes more pronounced with increasing harmonic order in agreement with the results of Ref. [34]. Comparing the spectrum for the Ehrenfest trajectory $\mathcal{R}_c(t)$ with $\mathcal{R}_c(t=0) = \mathcal{R}_{\rm eq} + |\alpha|\sigma$ with the spectrum that includes the sampling over a Schrödinger minimum uncertainty vibrational wave packet [Eqs. (18) and (19)] shows that the reduction of the HHG spectrum with increasing harmonic order persists [Fig. 3(b)]. Comparison between Figs. 3(a) and 3(b) also indicates that this effect does not strongly depend on the particular wave function to be sampled.

IV. SPECTRA FOR COMMENSURATE FREQUENCIES

When the oscillation frequency Ω of the coherent vibrational wave packet [Eq. (17)] becomes commensurate with the frequency ω_L of the laser driving the electronic dynamics, the coupling between the ionic and electronic dynamics is expected to be enhanced. This does not only apply to the case of a $1:1$ resonance, i.e., $\Omega = \omega_L$, which would require midinfrared driving fields but also higher-order resonances of commensurate frequencies, $\omega_L/\Omega = m/n$ (m, n: Integers). For H_2 and $\lambda_L = 800$ nm, this frequency ratio happens to be

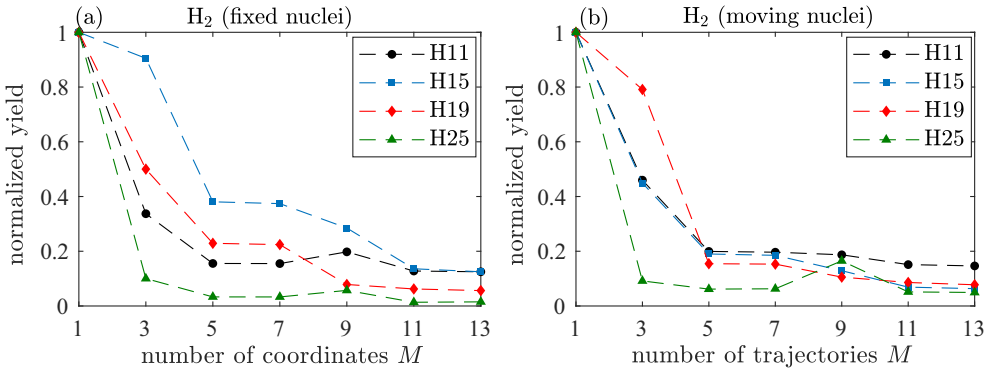

FIG. 5. Normalized intensity [$\sim S(\omega)$, linear scale] of selected harmonics between H11 and H25 as a function of the number of sampled $\mathcal{R}$ coordinates (left) and sampled trajectories $\mathcal{R}_j(t)$ (right).

close to the 5 : 2 resonance. For N_2 and $\lambda_L = 1147$ nm, a 3 : 1 resonance can be reached which also appears for HF at $\lambda_L = 800$ nm. At first glance, such a sensitivity to commensurate frequency ratios appears surprising as the electronic process of ionization and recombination occurs on an ultrafast time scale very short compared to the vibrational period $T_\Omega = 2\pi/\Omega$. It is, however, the superposition of these contributions from emission processes every optical half cycle over a time interval of several optical cycles that renders the spectrum sensitive to the frequency ratio Ω/ω_L. We explore in the following the impact of driving with commensurate frequencies on the high-order harmonic spectrum for the N_2, H_2, and HF molecules. For this simulation, we have increased the pulse length from six cycles to 14 cycles in order to narrow the spectral distribution of the pulse. For such longer laser-pulse interaction also the spectral width of the harmonic peaks becomes narrower and can be clearly identified up to the cutoff region of the spectrum. For commensurate frequencies the harmonic spectrum is fundamentally altered (Fig. 7). As the emission of harmonics from recollision events distributed over several optical cycles adds up coherently the information on the motion of the vibrational wave packet leaves a mark on

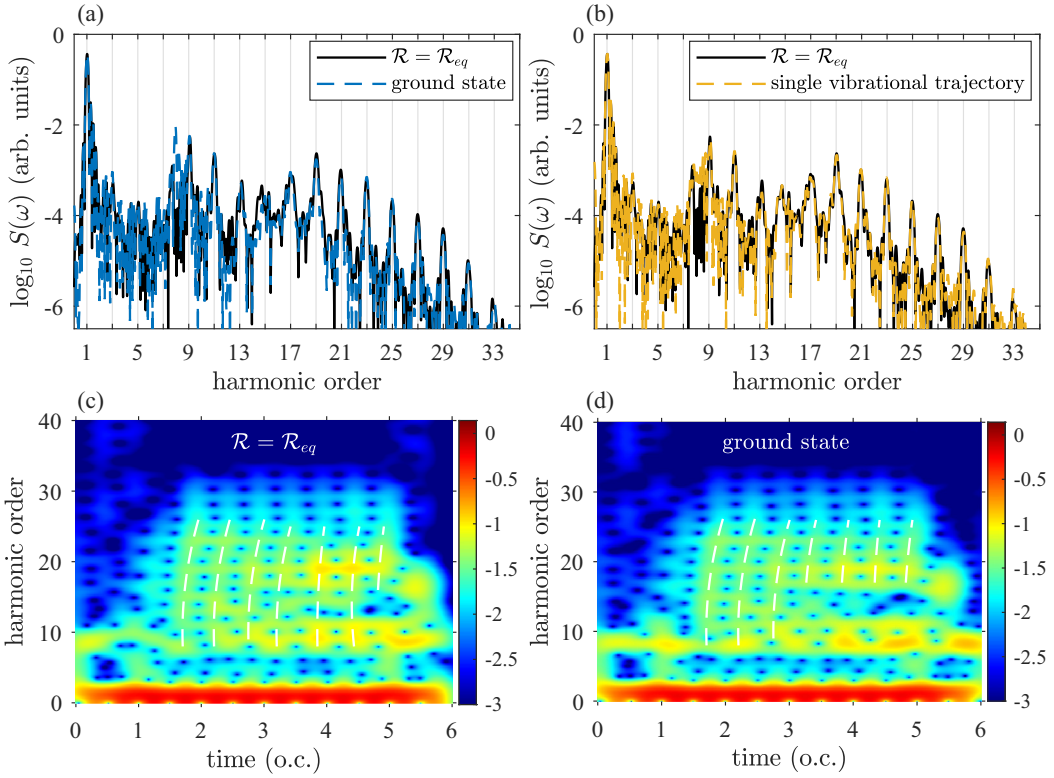

FIG. 6. Harmonic spectrum of F_2 driven by a six-cycle laser pulse ($\lambda_L = 800$ nm, $I_0 = 10^{14}$ W/cm^2). (a) Comparison between fixed nuclei at $\mathcal{R} = \mathcal{R}_{eq}$ and sampling over the stationary ground-state wave function [Eq. (13)]. (b) Comparison between $\mathcal{R} = \mathcal{R}_{eq}$ and a single Ehrenfest trajectory starting at the outer turning point $\mathcal{R}_0(t = 0) = \mathcal{R}_{eq} + |\alpha|\sigma$ with scaled amplitude $|\alpha| = 0.7$. (c), (d) Time-frequency analysis of HHG from F_2 for (c) fixed nuclei [black line in panel (a)] and (d) the sampling over the ground-state wave function [blue/gray dashed line in panel (a)]. The temporal width of the Gaussian window function in the Gabor transform is $\sigma_\tau = 0.5$ fs ($\approx$0.19 o.c.).

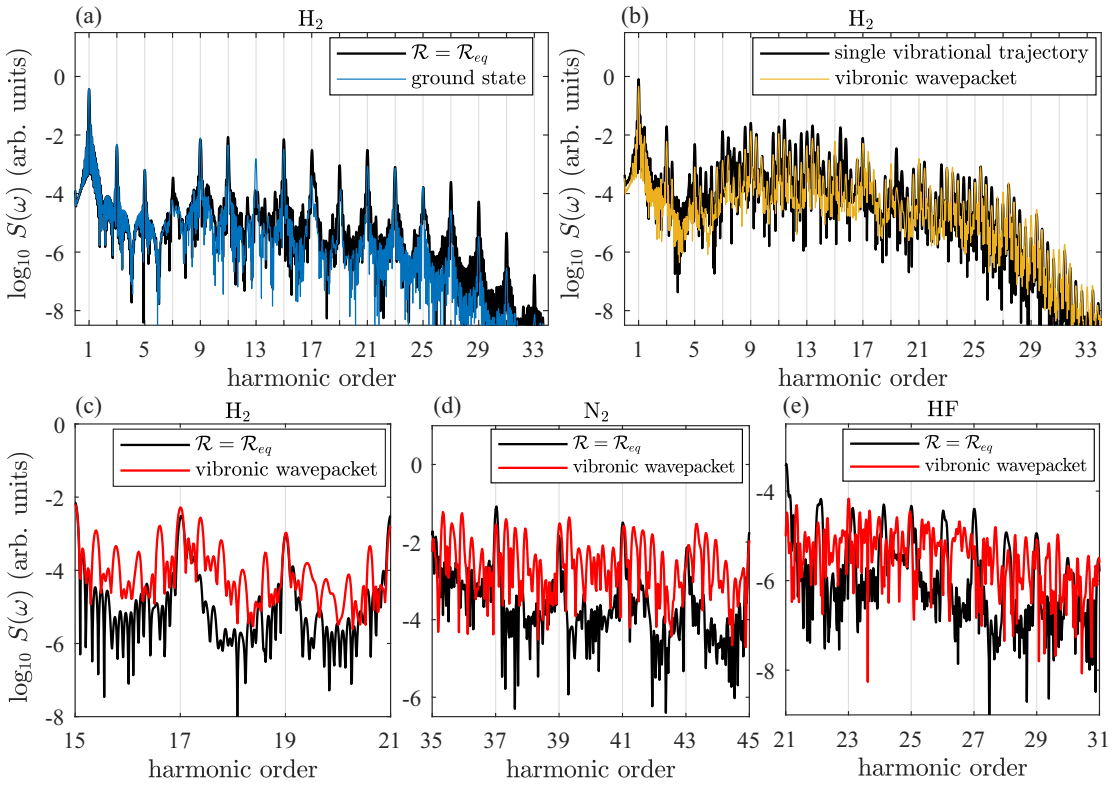

FIG. 7. Harmonics for laser driving frequencies ω_L (wavelength λ_L) commensurate with the frequency Ω of the vibrational wave packet: (a)–(c) H_2, (d) N_2, and (e) HF. In panels (c)–(e) we compare the HHG spectrum for fixed internuclear distance $\mathcal{R} = \mathcal{R}_{eq}$ with the result for the vibrational wave packet with sampling over the width of the vibrational wave function [five trajectories $\mathcal{R}_j(t)$]. (a) Comparison of complete spectra of H_2 irradiated with $\lambda_L = 800$ nm, $I_0 = 10^{14}$ W/cm^2, and $|\alpha| = 1.8$. Black line, fixed-ion calculation for $\mathcal{R} = \mathcal{R}_{eq}$; blue/dark gray line, vibrational ground state [Eq. (13)]. (b) As panel (a) but using Ehrenfest-TDDFT for single trajectory (black line) and for a vibrational wave-packet sampling by five trajectories $\mathcal{R}_j(t)$ [Eq. (19), orange/light gray line]. (c) Zoom-in of panels (a) and (b) for high-order harmonics of H_2. (d) N_2 with $\lambda_L = 1147$ nm, $I_0 = 10^{14}$ W/cm^2, and $|\alpha| = 2.8$. (e) HF with $\lambda_L = 800$ nm, $I_0 = 10^{14}$ W/cm^2, and $|\alpha| = 3.25$.

the spectrum. The energy spacing of $2\hbar\omega_L$ between successive HHG peaks is now filled by additional peaks spaced by $\hbar\Omega$. The appearance of additional peaks becomes clearly visible for all molecules investigated [Figs. 7(c)–7(e)] when compared with the spectrum in the fixed-ion approximation with $\mathcal{R} = \mathcal{R}_{eq}$. These additional peaks can be understood in terms of sidebands to the high-order harmonic peaks generated by the coupling between vibrational and electronic motion. It is important to note that a moderate anharmonicity resulting in a deviation from equispaced vibrational levels does not destroy the resonance effect as long as the spectral mismatch due to the anharmonicity lies within the linewidth of the driving pulse. The sampling over a minimum-uncertainty vibrational wave packet modifies the height of these resonant harmonics compared to that for a single Ehrenfest trajectory but qualitatively leaves the structure of the spectrum unchanged [Fig. 7(b)]. Obviously, the resonance is primarily governed by the classical vibrational nuclear motion while the spread of the quantum wave packet only influences the peak height of the sidebands, mostly causing a reduction. The appearance of these peaks at commensurate frequencies is a fairly robust classical resonance effect. Quantum coherence enters primarily through the requirement that the resonances are not suppressed by decoherence caused by random phases of the emission bursts accumulated in between subsequent half cycles. For F_2, quantum effects included via sampling over the wave function of the vibrational wave packet lead, unlike for H_2, only to a small change in the spectrum due to its small vibrational frequency (not shown). Pronounced resonant harmonics can be also observed for the (3:1) resonance of the strongly polar molecule HF [Fig. 7(e)]. Realization of such a resonance in this molecule is facilitated by the fact that the vibrational wave packet could be optically excited and steered. More generally, such vibrational wave packets can be excited by a variety of techniques including impulsive collisional excitation, Franck-Condon transitions, or impulsive stimulated Raman scattering [48]. The experimental observation of the commensurability effect on HHG appears thus feasible. Even when the subpeaks cannot be individually resolved, this resonance effect may facilitate an overall increase in the HHG yield in certain regions of the spectrum, e.g., between harmonics 35 and 45 in N_2 [Fig. 7(d)].

V. CONCLUSIONS

We have investigated the influence of vibrational motion on the HHG in several small molecules. The starting point is an Ehrenfest-TDDFT simulation within which the ionic motion follows the classical equations of motion with forces self-consistently determined from the time-dependent electronic density propagated by TDDFT. The influence of the shape and spread of the vibrational wave function on

the HHG is accounted for by the coherent superposition of the harmonic amplitudes of a distribution of trajectories sampling the wave function. One application addresses the HHG resulting from the excitation of node-free near-minimum uncertainty Schrödinger (or Glauber) wave packets which closely follow the classical vibrational motion. As expected, the influence of the vibrational degree of freedom is, in general, reduced with increasing mass of the molecular constituents. However, prominent resonance effects have been identified for commensurate frequencies the appearance of which is insensitive to the atomic masses involved. When a multiple of the frequency ω_L of the laser driving the strong-field ionization and recombination of the electron in the molecule is in resonance with a multiple of the vibrational frequency, i.e., $\omega_L/\Omega = m/n$, the standard harmonic spectra with spacing $2\hbar\omega_L$ between adjacent peaks is drastically altered. In case of such a resonance additional peaks spaced by $\sim\hbar\Omega \approx \frac{n}{m}\omega_L$ appear between harmonics which can lead, overall, to an increase of the HHG intensity in extended regions of the spectrum. A moderate anharmonicity of the vibrational spectrum does not destroy these resonance effects as long as the frequency mismatch lies within the Fourier width of the few-cycle infrared driving pulse. Experimental realization employing, for example, the impulse excitation of vibrational wave packets [48] appears within reach.

ACKNOWLEDGMENTS

This work has been supported by the doctoral college Grant No. FWF-1243 (Solids4Fun) of the Austrian Science Fund FWF (Fonds zur Förderung der wissenschaftlichen Forschung). The authors acknowledge the financial sponsorship provided by cofounding of Kharazmi University and Ministry of Science, Research, and Technology of the Islamic Republic of Iran and Austrian Fund OeAD under the IMPULSE Austria-Iran 15/2018 Program.

[1] P. B. Corkum and F. Krausz, Attosecond science, Nat. Phys. **3**, 381 (2007).
[2] F. Krausz and M. Ivanov, Attosecond physics, Rev. Mod. Phys. **81**, 163 (2009).
[3] M. Ivanov and E. Pisanty, Taking control of polarization, Nat. Photonics **8**, 501 (2014).
[4] F. Lépine, M. Y. Ivanov, and M. J. Vrakking, Attosecond molecular dynamics: Fact or fiction? Nat. Photonics **8**, 195 (2014).
[5] F. Calegari, G. Sansone, S. Stagira, C. Vozzi, and M. Nisoli, Advances in attosecond science, J. Phys. B: At. Mol. Opt. Phys. **49**, 062001 (2016).
[6] P. Peng, C. Marceau, and D. M. Villeneuve, Attosecond imaging of molecules using high harmonic spectroscopy, Nat. Rev. Phys. **1**, 144 (2019).
[7] J. Li, J. Lu, A. Chew, S. Han, J. Li, Y. Wu, H. Wang, S. Ghimire, and Z. Chang, Attosecond science based on high harmonic generation from gases and solids, Nat. Commun. **11**, 2748 (2020).
[8] J. Solanpää, J. A. Budagosky, N. I. Shvetsov-Shilovski, A. Castro, A. Rubio, and E. Räsänen, Optimal control of high-harmonic generation by intense few-cycle pulses, Phys. Rev. A **90**, 053402 (2014).
[9] P. Ranitovic, C. W. Hogle, P. Rivière, A. Palacios, X.-M. Tong, N. Toshima, A. González-Castrillo, L. Martin, F. Martín, M. M. Murnane *et al.*, Attosecond vacuum uv coherent control of molecular dynamics, Proc. Natl. Acad. Sci. USA **111**, 912 (2014).
[10] P. Lan, M. Ruhmann, L. He, C. Zhai, F. Wang, X. Zhu, Q. Zhang, Y. Zhou, M. Li, M. Lein *et al.*, Attosecond Probing of Nuclear Dynamics with Trajectory-Resolved High-Harmonic Spectroscopy, Phys. Rev. Lett. **119**, 033201 (2017).
[11] P. B. Corkum, Plasma Perspective on Strong Field Multiphoton Ionization, Phys. Rev. Lett. **71**, 1994 (1993).
[12] K. J. Schafer, B. Yang, L. F. DiMauro, and K. C. Kulander, Above Threshold Ionization Beyond the High Harmonic Cutoff, Phys. Rev. Lett. **70**, 1599 (1993).
[13] J. L. Krause, K. J. Schafer, and K. C. Kulander, High-Order Harmonic Generation from Atoms and Ions in the High Intensity Regime, Phys. Rev. Lett. **68**, 3535 (1992).
[14] X.-M. Tong and S.-I. Chu, Theoretical study of multiple high-order harmonic generation by intense ultrashort pulsed laser fields: A new generalized pseudospectral time-dependent method, Chem. Phys. **217**, 119 (1997).
[15] C. Ruiz, L. Plaja, L. Roso, and A. Becker, *ab initio* Calculation of the Double Ionization of Helium in a Few-Cycle Laser Pulse Beyond the One-Dimensional Approximation, Phys. Rev. Lett. **96**, 053001 (2006).
[16] A. Palacios, T. N. Rescigno, and C. W. McCurdy, Cross sections for short-pulse single and double ionization of helium, Phys. Rev. A **77**, 032716 (2008).
[17] J. Feist, S. Nagele, R. Pazourek, E. Persson, B. I. Schneider, L. A. Collins, and J. Burgdörfer, Nonsequential two-photon double ionization of helium, Phys. Rev. A **77**, 043420 (2008).
[18] E. Runge and E. K. U. Gross, Density-Functional Theory for Time-Dependent Systems, Phys. Rev. Lett. **52**, 997 (1984).
[19] X.-M. Tong and Shih-I Chu, Time-dependent density-functional theory for strong-field multiphoton processes: Application to the study of the role of dynamical electron correlation in multiple high-order harmonic generation, Phys. Rev. A **57**, 452 (1998).
[20] J. Caillat, J. Zanghellini, M. Kitzler, O. Koch, W. Kreuzer, and A. Scrinzi, Correlated multielectron systems in strong laser fields: A multiconfiguration time-dependent Hartree-Fock approach, Phys. Rev. A **71**, 012712 (2005).
[21] F. Lackner, I. Březinová, T. Sato, K. L. Ishikawa, and J. Burgdörfer, High-harmonic spectra from time-dependent two-particle reduced-density-matrix theory, Phys. Rev. A **95**, 033414 (2017).
[22] M. Lewenstein, P. Balcou, M. Y. Ivanov, A. L'Huillier, and P. B. Corkum, Theory of high-harmonic generation by low-frequency laser fields, Phys. Rev. A **49**, 2117 (1994).

[23] M. Lein, Attosecond Probing of Vibrational Dynamics with High-Harmonic Generation, Phys. Rev. Lett. **94**, 053004 (2005).

[24] W. Qu, Z. Chen, Z. Xu, and C. H. Keitel, Nuclear correlation in ionization and harmonic generation of h_2+ in short intense laser pulses, Phys. Rev. A **65**, 013402 (2001).

[25] C. B. Madsen and L. B. Madsen, High-order harmonic generation from arbitrarily oriented diatomic molecules including nuclear motion and field-free alignment, Phys. Rev. A **74**, 023403 (2006).

[26] A. D. Bandrauk, S. Chelkowski, S. Kawai, and H. Lu, Effect of Nuclear Motion on Molecular High-Order Harmonics and on Generation of Attosecond Pulses in Intense Laser Pulses, Phys. Rev. Lett. **101**, 153901 (2008).

[27] A. D. Bandrauk, S. Chelkowski, and H. Lu, Signatures of nuclear motion in molecular high-order harmonics and in the generation of attosecond pulse trains by ultrashort intense laser pulses, J. Phys. B: At. Mol. Opt. Phys. **42**, 075602 (2009).

[28] C. Liu, Z. Zeng, P. Wei, P. Liu, R. Li, and Z. Xu, Driving-laser wavelength dependence of high-order harmonic generation in H_{2+} molecules, Phys. Rev. A **81**, 033426 (2010).

[29] H. Ahmadi, A. Maghari, H. Sabzyan, A. R. Niknam, and M. Vafaee, Effect of nuclear motion on high-order-harmonic generation of H_{2+} in intense ultrashort laser pulses, Phys. Rev. A **90**, 043411 (2014).

[30] S. Baier, C. Ruiz, L. Plaja, and A. Becker, Nonsequential double ionization of the hydrogen molecule in a few-cycle laser pulse, Phys. Rev. A **74**, 033405 (2006).

[31] X. Yuan, P. Wei, C. Liu, X. Ge, Y. Zheng, Z. Zeng, and R. Li, Effect of nuclear motion on spectral broadening of high-order harmonic generation, Opt. Express **24**, 8194 (2016).

[32] X.-B. Bian and A. D. Bandrauk, Probing Nuclear Motion by Frequency Modulation of Molecular High-Order Harmonic Generation, Phys. Rev. Lett. **113**, 193901 (2014).

[33] L. He, Q. Zhang, P. Lan, W. Cao, X. Zhu, C. Zhai, F. Wang, W. Shi, M. Li, X.-B. Bian, P. Lu, and A. D. Bandrauk, Monitoring ultrafast vibrational dynamics of isotopic molecules with frequency modulation of high-order harmonics, Nat. Commun. **9**, 1108 (2018).

[34] X. Chu and G. C. Groenenboom, Time-dependent density-functional-theory calculation of high-order-harmonic generation of H_2, Phys. Rev. A **85**, 053402 (2012).

[35] S. Baker, J. S. Robinson, C. Haworth, H. Teng, R. Smith, C. Chirilă, M. Lein, J. Tisch, and J. P. Marangos, Probing proton dynamics in molecules on an attosecond time scale, Science **312**, 424 (2006).

[36] X. Chu and Shih-I Chu, Self-interaction-free time-dependent density-functional theory for molecular processes in strong fields: High-order harmonic generation of H_2 in intense laser fields, Phys. Rev. A **63**, 023411 (2001).

[37] R. Baer, D. Neuhauser, P. R. Ždánská, and N. Moiseyev, Ionization and high-order harmonic generation in aligned benzene by a short intense circularly polarized laser pulse, Phys. Rev. A **68**, 043406 (2003).

[38] D. A. Telnov and Shih-I Chu, Effects of multiple electronic shells on strong-field multiphoton ionization and high-order harmonic generation of diatomic molecules with arbitrary orientation: An all-electron time-dependent density-functional approach, Phys. Rev. A **80**, 043412 (2009).

[39] S. Petretti, Y. V. Vanne, A. Saenz, A. Castro, and P. Decleva, Alignment-Dependent Ionization of $\mathbf{N}_2$, $\mathbf{O}_2$, and CO_2 in Intense Laser Fields, Phys. Rev. Lett. **104**, 223001 (2010).

[40] E. Penka Fowe and A. D. Bandrauk, Nonperturbative time-dependent density-functional theory of ionization and harmonic generation in OCS and CS_2 molecules with ultrashort intense laser pulses: Intensity and orientational effects, Phys. Rev. A **84**, 035402 (2011).

[41] D. Dundas, Multielectron effects in high harmonic generation in N2 and benzene: Simulation using a non-adiabatic quantum molecular dynamics approach for laser-molecule interactions, J. Chem. Phys. **136**, 194303 (2012).

[42] T. Kunert and R. Schmidt, Non-adiabatic quantum molecular dynamics: General formalism and case study H_{2+} in strong laser fields, Eur. Phys. J. D **25**, 15 (2003).

[43] D. Dundas, Accurate and efficient non-adiabatic quantum molecular dynamics approach for laser–matter interactions, J. Phys. B: At. Mol. Opt. Phys. **37**, 2883 (2004).

[44] F. Calvayrac, P.-G. Reinhard, E. Suraud, and C. Ullrich, Nonlinear electron dynamics in metal clusters, Phys. Rep. **337**, 493 (2000).

[45] A. Castro, M. A. L. Marques, J. A. Alonso, G. F. Bertsch, and A. Rubio, Excited states dynamics in time-dependent density functional theory - high-field molecular dissociation and harmonic generation, Eur. Phys. J. D **28**, 211 (2004).

[46] A. Wardlow and D. Dundas, High-order-harmonic generation in benzene with linearly and circularly polarized laser pulses, Phys. Rev. A **93**, 023428 (2016).

[47] P. Mulholland and D. Dundas, High-order harmonic generation from highly excited states in acetylene, Phys. Rev. A **97**, 043428 (2018).

[48] W. Li, X. Zhou, R. Lock, S. Patchkovskii, A. Stolow, H. C. Kapteyn, and M. M. Murnane, Time-resolved dynamics in N2O4 probed using high harmonic generation, Science **322**, 1207 (2008).

[49] A. L'Huillier, L. A. Lompré, G. Mainfray, and C. Manus, High-order harmonic generation in rare gases, in *Atoms in Intense Laser Fields*, edited by M. Gavrila (Academic, New York, 1992), pp. 139–206.

[50] A. Abedi, N. T. Maitra, and E. K. U. Gross, Exact Factorization of the Time-Dependent Electron-Nuclear Wave Function, Phys. Rev. Lett. **105**, 123002 (2010).

[51] C. Li, R. Requist, and E. K. U. Gross, Energy, Momentum, and Angular Momentum Transfer between Electrons and Nuclei, Phys. Rev. Lett. **128**, 113001 (2022).

[52] L. S. Cederbaum, Born-Oppenheimer approximation and beyond for time-dependent electronic processes, J. Chem. Phys. **128**, 124101 (2008).

[53] C. Hartwigsen, S. Goedecker, and J. Hutter, Relativistic separable dual-space gaussian pseudopotentials from H to RN, Phys. Rev. B **58**, 3641 (1998).

[54] J. P. Perdew, K. Burke, and M. Ernzerhof, Generalized Gradient Approximation Made Simple, Phys. Rev. Lett. **77**, 3865 (1996).

[55] M. Schlipf and F. Gygi, Optimization algorithm for the generation of ONCV pseudopotentials, Comput. Phys. Commun. **196**, 36 (2015).

[56] M. A. Marques, A. Castro, G. F. Bertsch, and A. Rubio, Octopus: A first-principles tool for excited electron–ion dynamics, Comput. Phys. Commun. **151**, 60 (2003).

[57] N. Tancogne-Dejean, M. J. Oliveira, X. Andrade, H. Appel, C. H. Borca, G. Le Breton, F. Buchholz, A. Castro, S. Corni, A. A. Correa *et al.*, Octopus, a computational framework for exploring light-driven phenomena and quantum dynamics in extended and finite systems, J. Chem. Phys. **152**, 124119 (2020).

[58] E. Schrödinger, Der stetige übergang von der mikro- zur makromechanik, Naturwissenschaften **14**, 664 (1926).

[59] R. J. Glauber, Photon Correlations, Phys. Rev. Lett. **10**, 84 (1963).

[60] A. Belfakir, Y. Hassouni, and E. M. Curado, Construction of coherent states for morse potential: A SU (2)-like approach, Phys. Lett. A **384**, 126553 (2020).

[61] A. Belfakir, E. M. Curado, and Y. Hassouni, Time evolution and anti-bunching effect of diatomic molecules coherent states, Ann. Phys. (NY) **423**, 168331 (2020).

[62] S. Kais and R. D. Levine, Coherent states for the morse oscillator, Phys. Rev. A **41**, 2301 (1990).

[63] M. Angelova and V. Hussin, Generalized and Gaussian coherent states for the Morse potential, J. Phys. A: Math. Theor. **41**, 304016 (2008).

[64] M. Dantus, R. M. Bowman, and A. H. Zewail, Femtosecond laser observations of molecular vibration and rotation, Nature (London) **343**, 737 (1990).

[65] E. Goll, G. Wunner, and A. Saenz, Formation of Ground-State Vibrational Wave Packets in Intense Ultrashort Laser Pulses, Phys. Rev. Lett. **97**, 103003 (2006).

[66] A. Saenz, Enhanced ionization of molecular hydrogen in very strong fields, Phys. Rev. A **61**, 051402(R) (2000).

[67] Z. Wei, J. Li, L. Wang, S. T. See, M. H. Jhon, Y. Zhang, F. Shi, M. Yang, and Z.-H. Loh, Elucidating the origins of multimode vibrational coherences of polyatomic molecules induced by intense laser fields, Nat. Commun. **8**, 735 (2017).

[68] D. Gabor, Theory of communication. Part 1: The analysis of information, J. Inst. Electr. Eng. **93**, 429 (1946).

[69] C. C. Chirilă, I. Dreissigacker, E. V. van der Zwan, and M. Lein, Emission times in high-order harmonic generation, Phys. Rev. A **81**, 033412 (2010).

[70] J. C. Tully, Molecular dynamics with electronic transitions, J. Chem. Phys. **93**, 1061 (1990).